Supporting information: Understanding the role of acidity on the surface exchange reaction in mixed conductors: What is the effect of surface hydration?

David M. Schwenkel,[a] Roger A. De Souza,[a] and George F. Harrington,*[a,b]

[a] *Institute of Physical Chemistry, RWTH Aachen University, Germany*
[b] *Department of Chemistry, University of Bath, UK*

* *E-mail: gh778@bath.ac.uk*

1 X-ray diffraction

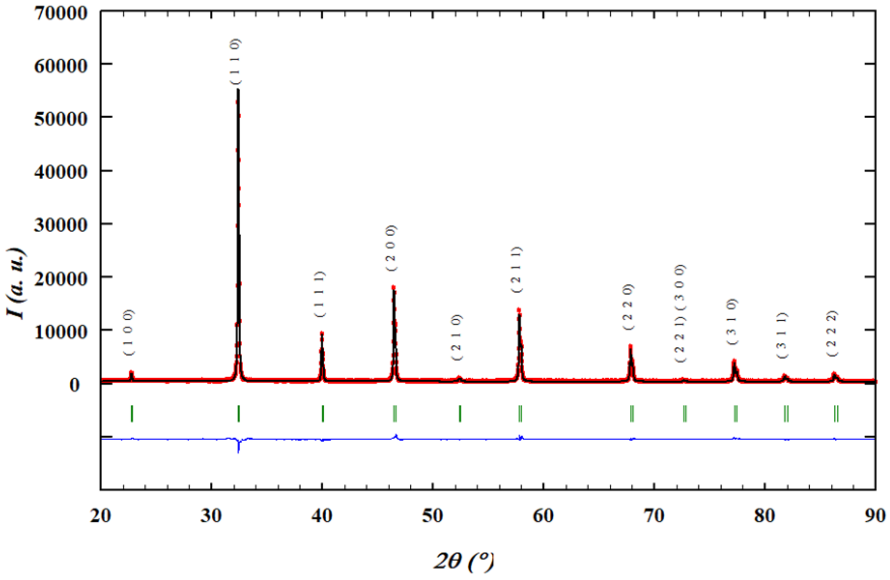

Figure S1: XRD pattern of $SrTi_{0.65}Fe_{0.35}O_{3-\delta}$ porous pellet after sintering at 1100°C. The pattern was measured on a Bruker D2 Phaser instrument using Cu K_α radiation in Bragg-Brentano geometry. The pattern was fitted using the Le Bail method (FullProf software), to confirm the $Pm\bar{3}m$ space group and a lattice parameter of 3.902Å.

2 Scanning electron microscopy

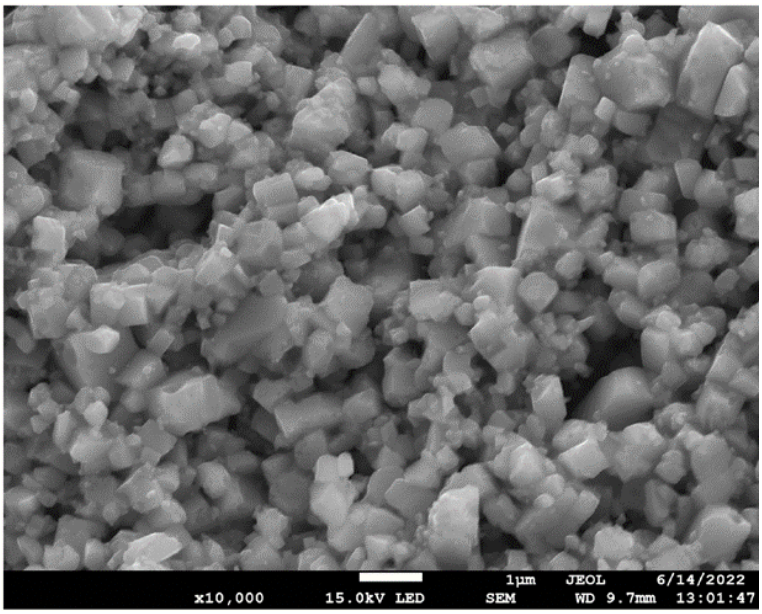

Figure S2: Representative SEM image of the STF microstructure.

Composition	Sr	Ti	Fe	O
Target	1.00	0.65	0.35	2.825
Measured	1.00	0.67	0.36	3.43

Table S1: Elemental ratios for STF from EDX measurements.

The elemental composition was determined by energy dispersive X-ray spectroscopy (EDX, Oxford Instruments) and analysed using the AZtec software. The stoichiometry was normalised to strontium and compare to the target calculated as $SrTi_{1-x}Fe_xO_{3-(x/2)+\delta}$ with $\delta = 0$. The results are given in Table S1. The Sr:Ti:Fe ratios are in good agreement with the target composition. There is a significant deviation for the oxygen stoichiometry, however given the semi-quantitative nature of EDX measurements, especially for light elements, this was not further regarded.

3 Surface area calculation

The grain size distribution was determined by measuring individual grain sizes in the *ImageJ* software. The resultant histogram is shown in Figure S3. The data are fit with a log-normal

distribution, as is commonly used to describe the grain-size distribution in polycrystals. [1]

$$f(l_{\text{grain}}) = \frac{N}{l_{\text{grain}}\omega\sqrt{2\pi}} \cdot e^{-\frac{\left(\ln\frac{l_{\text{grain}}}{l_{\text{c}}}\right)^2}{2\omega^2}}, \quad \text{for } l_{\text{grain}} \in (0, +\infty) \tag{1}$$

The expected value, μ, and the standard deviation, σ, of the grain size are given by Equation 2 and Equation 3 from the fit parameters, respectively, and given in Table S2.

$$\mu = e^{\ln(l_c)\frac{\omega^2}{2}} \tag{2}$$

$$\sigma = \mu \cdot \sqrt{e^{\omega^2} - 1} \tag{3}$$

The surface area was calculated assuming a cubic grain morphology, which seems most appropriate from the SEM imaging. The surface area was calculated according to Equation 4 from the sum of the volume (ΣV) and surface area (ΣA) of all grains that were measured for the grain size distribution analysis, and corrected for the porosity of the sample as measured geometrically (V_V).

$$S_V = \frac{\sum A}{\sum V \cdot (1 - V_V)} \tag{4}$$

Table S2: Grain size, l_{grain}, specific surface area, S_V, and volume fraction porosity, V_V.

l_{grain} [μm]		S_V [cm^{2}cm^{-3}]	V_V [%]
μ	$\pm\sigma$		
0.36	0.16	143,477	32.24

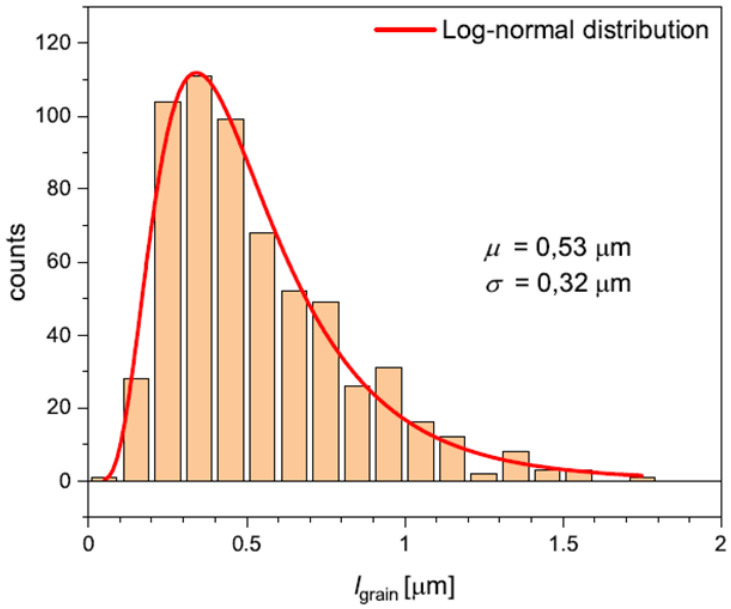

Figure S3: Grain size distribution for porous STF taken from SEM imaging with log-normal distribution.

4 Electrical conductivity relaxation

The surface exchange kinetics were assessed using electrical conductivity relaxation (ECR) on porous bars. The p_{O_2} was rapidly changed from 0.2 to 0.1 atm and 0.1 to 0.2 atm using a 4-way valve, in a temperature range between 300-500°C. Figure S4 shows a typical measurement program of non-infiltrated STF.

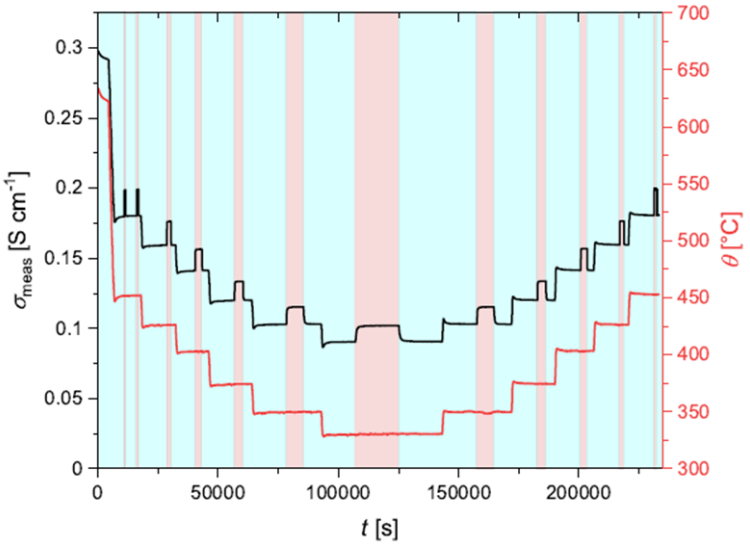

Figure S4: ECR measurement of non-infiltrated STF. Blue regions indicate $p_{O_2} = 0.1$ atm and red regions indicate $p_{O_2} = 0.2$ atm.

The normalised conductivity, σ_0, for each relaxation was fitted to an exponential delay function to determine k_{chem}, as shown in Figure S5. It was found that the transient data could not be satisfactorily described by an exponential function with a single time constant. This is unsurprising due to the large distribution of grain sizes in the bars, which would lead to a distribution of time constants for a constant surface k_{chem}. To account for this distribution, an expression with two time constants was used,

$$\sigma_{\text{norm}} = A_1 \cdot (1 - e^{-\frac{t}{\tau_1}}) + (1 - A_2) \cdot (1 - e^{-\frac{t}{\tau_2}}), \tag{5}$$

where τ_1 and τ_2 are the two time constants and A_1 is a weighting factor. The average time constant for the relaxation was calculated according to

$$\tau = A_1 \cdot \tau_1 + (1 - A_2) \cdot \tau_2. \tag{6}$$

The surface exchange rate was then calculated according to Equation 7 using τ and the specific surface area, S_V, and the volume fraction porosity, V_V, given in Table S3.

$$k_{\text{chem}} = \frac{(1 - V_V)}{S_V \cdot \tau} \tag{7}$$

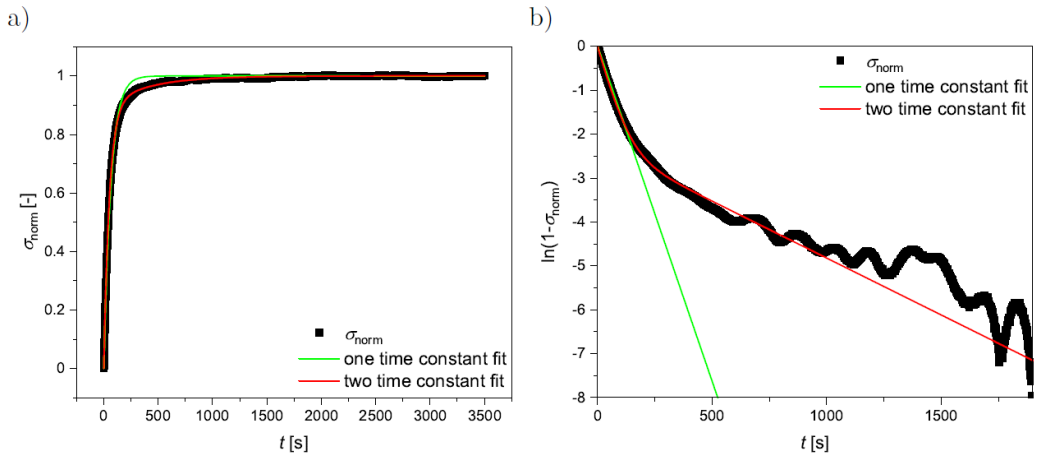

Figure S5: Representative electrical conductivity relaxation transient of non-infiltrated STF at 375°C as the atmosphere is switched from $p_{O_2} = 0.1$ atm to $p_{O_2} = 0.2$ atm. The lines indicate fitting with either one or two time constants. The data is plotted as a) σ_{norm} as a function of time or b) $\ln(1-\sigma_{norm})$ as a function of time.

As seen in Figure S5, Equation 5 describes the data well. Although a broad distribution of relaxation times would be expected from a board distribution of grain sizes, Equation 5 was able to provide a satisfactory fit, while adding additional exponential functions would be potentially over-fitting the data.

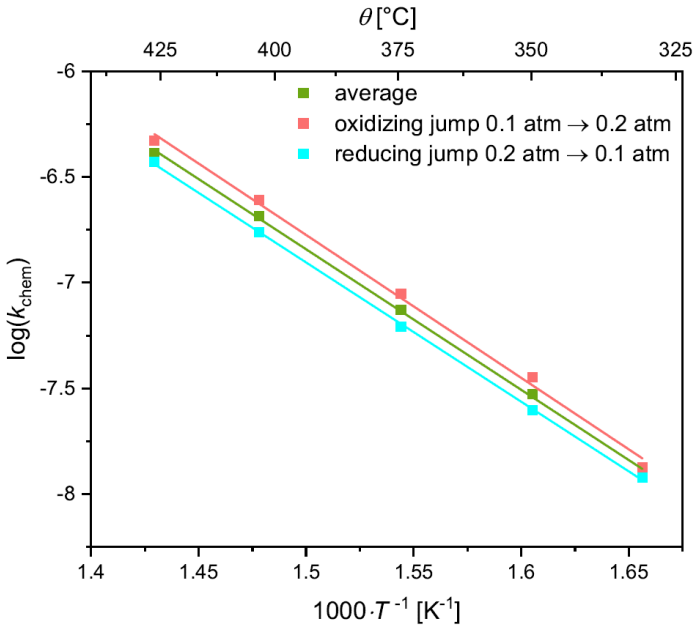

Figure S6: k_{chem} against inverse temperature for an oxidizing and reducing jump between $p_{O_2} = 0.1$ atm and $p_{O_2} = 0.2$ atm, of non-infiltrated STF; the errors on k_{chem} are smaller than the symbols and therefore not displayed.

The surface exchange coefficients for oxidizing and reducing jumps for non-infiltrated STF are presented in an Arrhenius plot in Figure S6. The surface exchange rate for the oxidizing jump is consistently higher than for the reducing jump. This is expected, as the equilibria with the gas phase, and therefore the concentration of point defects, is different for each type of jump. The relaxation transient is mainly determined by the initial reaction rate, which will depend on the initial p_{O_2}. It is not unsurprising that k_{chem} is higher for $p_{O_2} = 0.1$ atm than at $p_{O_2} = 0.2$ atm, as both the electron and oxygen vacancies concentrations should be higher. [2] These results align with the findings of Merkle *et al.*, who conducted an extensive study on the p_{O_2} dependence of oxygen surface exchange in weakly doped $SrTiO_3$. [3]

One of the checks we performed to ensure that the measured values of k_{chem} are representative of the STF surface exchange was to compare to the published literature. Figure S7 compares the ECR measurements of non-infiltrated $SrTi_{0.65}Fe_{0.35}O_{3-\delta}$ (STF35) in this work with literature values of k_{chem} measured using films of STF35 grown via pulsed laser deposition (PLD). [4–6] There is substantial scatter across the literature measurements, which can be ascribed to the different growth conditions of the films: some grown below the crystallisation temperature and crystallising in post-treatment, others grown at or above the crystallisation temperature. The measured k_{chem} values in this work lie within the scatter of the previous literature. The activation energy obtained in this work, $E_A = 1.33 \pm 0.02$ is in good agreement with the that found by Chen et al., [4] $E_A = 1.28$ and Skiba *et al.*, [6] $E_A = 1.30 \pm 0.09$, on crystalline films grown at high temperature and on amorphous films crystallised in post treatment, respectively.

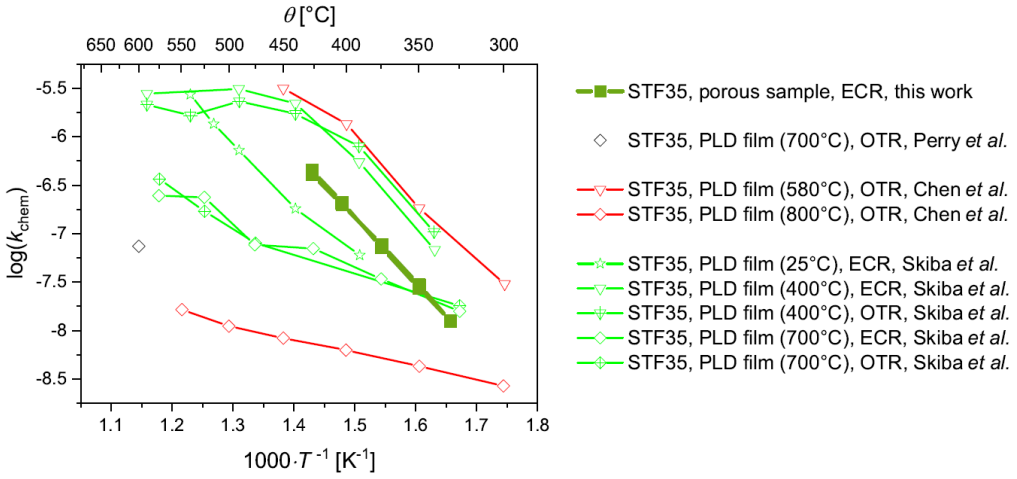

Figure S7: k_{chem} values from this study in comparison to literature values from Perry et al., [5] Chen et al., [4], and Skiba et al. [6] on STF35 thin films from electrical conductivity relaxation (ECR) and optical transmission relaxation (OTR) measurements.

The solutions used for infiltration is applied to the centre of the bar-shaped samples after gold electrodes had already been attached and the native surface measured by ECR. This had the advantage that the bars could be supported using the wire contacts rather than lying on a surface where there may have been a potential for the solution to pool due to capillary action. Furthermore, the ethanol-based solution readily wets the STF material and upon applying the 60 µL of solution, is immediately absorbed into the porous structure, forming a visibly uniform coating

Figure S8 shows representative conductivity relaxation transients of non-infiltrated STF and STF infiltrated with either CaO or SiO_2 at 375°C plotted on a semi-log scale. As previously discussed, the relaxation transient displays a distribution of relaxation times due to the grain size distribution. There is no obvious difference in the shape of the distribution transients with infiltration, which indicates that the effect of the infiltrated species on k_{chem} is uniform over the surface of the STF. This is in agreement with previous reports on PCO. [7]

As the change in the relaxation behaviour is uniform for all the relaxation times, this suggests that the surface is altered uniformly, and that the infiltrated species is highly dispersed on the surface. Here, the loading used was 0.5 at.% based off the mass of the porous bars. From the surface area calculations (Table S2), this corresponds to approximately half a monolayer for a uniform coating. This was not verified experimentally, however, as previous studies reported that highly dispersed oxides infiltrated in this way which are responsible for the change in k_{chem} could not be observed by SEM or TEM imaging. [7]

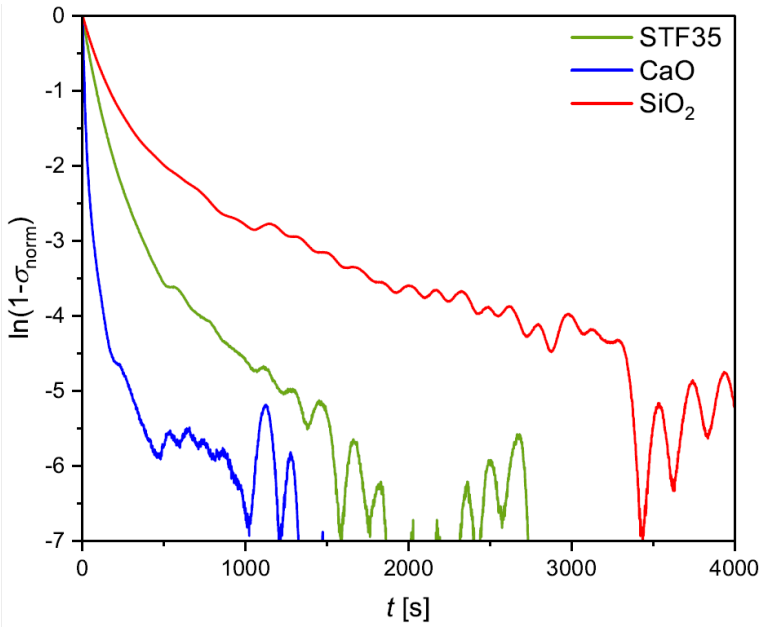

Figure S8: Conductivity relaxation curves from between $p_{O_2} = 0.1$ atm to $p_{O_2} = 0.2$ atm of both non-infiltrated STF and surface infiltrated STF with binary oxides at 375°C.

5 Steady-state conductivity

Figure S9a shows the steady-state conductivity after the STF bar had reached equilibrium at $p_{O_2} = 0.1$ atm and $p_{O_2} = 0.2$ atm. Due to the porous nature of the samples, the conductivity, σ, was corrected for the porosity using the Bruggeman effective-medium approximation. [8]

$$(1 - V_V)\,\frac{\sigma_t - \sigma_{\text{meas}}}{\sigma_t + 2\sigma_{\text{meas}}} + V_V \frac{\sigma_{\text{air}} - \sigma_{\text{meas}}}{\sigma_{\text{air}} + 2\sigma_{\text{meas}}} = 0 \tag{8}$$

Equation 8 was solved for σ, where σ_{meas} is the measured conductivity and σ_{air} is set to zero as the fractional the conductivity of the pores.

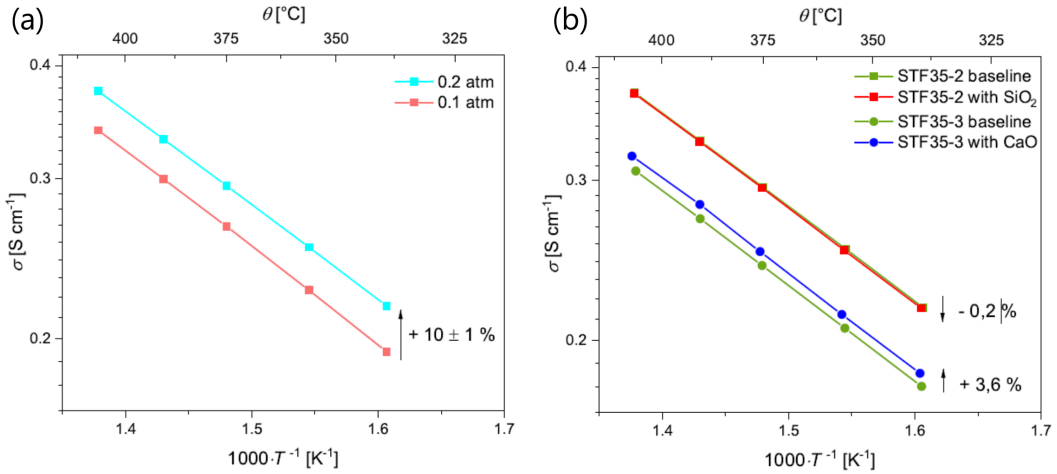

Figure S9: Conductivity for a) non-infiltrated STF at $p_{O_2} = 0.1$ atm and $p_{O_2} = 0.2$ atm and b) for both infiltrated species at $p_{O_2} = 0.2$ atm.

All samples, included those with a modified surface, displayed a constant activation of (0.269 ± 0.003) eV. The conductivity increases by (10 ± 1)% from $p_{O_2} = 0.1$ atm to $p_{O_2} = 0.2$ atm which corresponds to a p_{O_2} power law dependence of +1/6. This is consistent with the hole concentration from the defect model [2] confirming that STF exhibits predominantly p-type conductivity and that the non-stoichiometry change in the samples is being tracked during the ECR measurements.

In the previous study on PCO by Nicollet *et al.*, small, yet systematic, changes in the conductivity were observed after infiltration, with basic oxides resulting in an increase of up to 25% and acidic oxides resulting in a slight decrease in the conductivity. [7] It was argued that this behaviour was consistent with electron accumulation or depletion in the subsurface due to band bending caused by the basic and acidic species respectively. More recent studies by Riedl *et al.* performed on PCO thin films with acidic and basic coatings, however, showed no increase or decrease in the Pr^{3+}/ Pr^{4+} ratio, used as a proxy for the electron concentration, from X-ray photoelectron spectroscopy (XPS) measurments. [9] Moreover, the authors did not observe changes in the conductivity of the PCO films with different coatings.

Figure S9b shows the change in the conductivity of STF in this study after infiltration with CaO or SiO_2. A small increase in the conductivity of 3.6% was observed for CaO infiltration and a decrease of 0.2% for the SiO_2 infiltration, although this may be within the experimental uncertainty. While it is not exactly clear what the cause of the change in the conductivity is, the results in this study on porous STF bars display the same behaviour as the previous study on PCO.

6 Electron transfer model

A band bending model has been proposed by Nicollet *et al.* to explain the effect of acidity of infiltrated oxides on the surface exchange of MIECs. [7] This model assumes that the rate determining step (RDS) for oxygen exchange is electron transfer from the conduction band. Figure S10 demonstrates the concept schematically, now applied to the STF system, where previous studies have also indicated the RDS is electron transfer. [3, 10, 11]

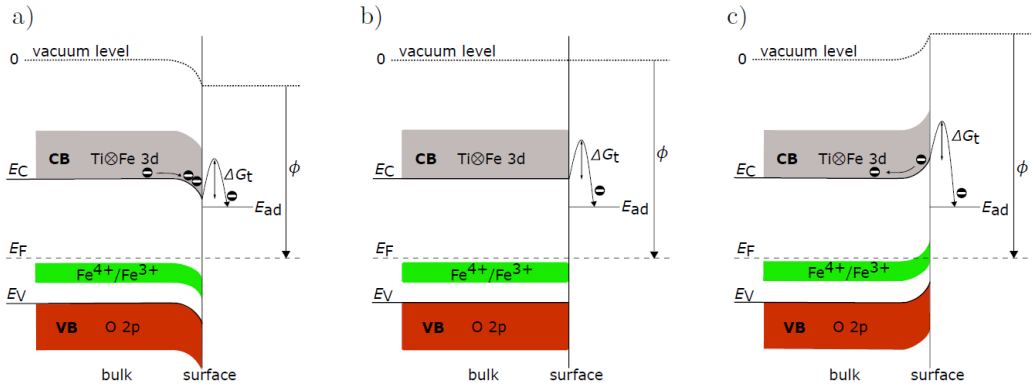

Figure S10: Effect of acidic and basic binary oxides on the band structure of STF, a) for a more basic oxide, b) for an non-infiltrated surface and c) for a more acidic oxide.

In Figure S10, the position of the Fermi level of the STF is pinned to that of the infiltrated binary oxide, the position of which is correlated to the Smith acidity and the work function. [12] For basic oxides, downwards band-bending occurs in the STF leading to the accumulation of electrons at the surface and in the sub-surface, while for acidic oxides, upwards band-bending occurs leading to the depletion of electrons.

For semiconducting oxides, where electron transfer is the RDS, the surface exchange may be described by

$$k_{\mathrm{s}}^{*} = d_{\mathrm{t}} v_0 \sqrt{aO_2} \frac{[\mathrm{e}_{\mathrm{s}}'][\mathrm{s}_{\mathrm{ad}}]}{[\mathrm{O}_{\mathrm{b}}]} e^{-(\Delta \mathrm{G}_{\mathrm{t}}^{\ddagger} + \Delta \mathrm{G}_{\mathrm{ad}})/k_{\mathrm{B}}T} \tag{9}$$

where d_{t} is the distance over which the electron transfer takes place, v_0 is the attempt frequency, and aO_2 is the oxygen activity. $[\mathrm{e}_{\mathrm{s}}']$, $[s_{\mathrm{ad}}]$, and $[\mathrm{O}_{\mathrm{b}}]$ are the concentrations of electrons at the surface, surface adsorption sites, and oxide ions in the bulk, respectively. $\Delta \mathrm{G}_t^{\ddagger}$ is the Gibbs energy for electron transfer, which could either be the difference in the energy barrier between the conduction band and the adsorbed oxygen Fermi level, or an activation barrier that must be overcome. $\Delta \mathrm{G}_{\mathrm{ad}}$ is the Gibbs energy for oxygen adsorption from gas species onto an adsorption site. The modified electron concentration at the surface, $[\mathrm{e}_{\mathrm{s}}']$, would then be described by the following relation where the space-charge potential ϕ_0, is equal to the offset between the Fermi levels of the MIEC oxide and of the infiltrated species.

$$[\mathrm{e}_{\mathrm{s}}'] = [\mathrm{e}_{\mathrm{b}}'] \exp\left(\frac{e\phi_0}{k_{\mathrm{B}}T}\right) \tag{10}$$

Figure S11 shows an attempt to fit the previously published PCO data and the STF data from this study using Equations 9 and 10 and the bulk defects models. [2,13,14] k_{chem} data from ECR measurements are converted to the equilibrium or tracer surface exchange coefficient k^* according to [15]

$$k_{\mathrm{chem}} = t_{\mathrm{e}} \frac{1}{2} \frac{d \ln(p_{\mathrm{O}_2})}{d \ln([\mathrm{O}_O^{\times}])} k_{\mathrm{s}}^{*} \tag{11}$$

where t_e is the electron transference number, and $[\mathrm{O}_O^{\times}]$ is the bulk oxygen concentration. The fitted differences in the work-function of the base MIEC and the infiltrated oxides are shown in Table S3. Although the change in magnitude of k_{s}^{*} with different infiltrated species can be

reproduced, with physically reasonable differences in the work-function, the fits are relatively poor, even for the non-infiltrated data, and Equation 10 results in a change in the activation energy that is not observed in the data.

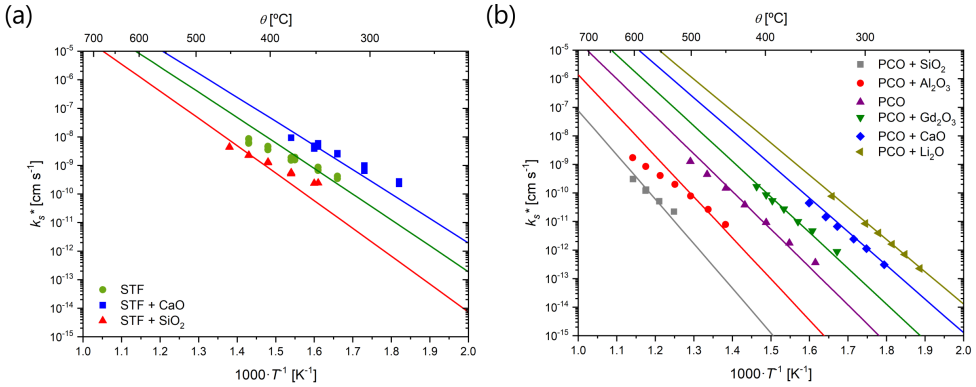

Figure S11: k_s^* of (a) STF (this work) and (b) PCO (Nicollet *et al.* [7]) converted from k_{chem} values from ECR measurements using thermodynamic factors and fitted using Equations 9 and 10. The values for the space charge potential, ϕ_0 are given in Table S3.

Table S3: Values used for ϕ_0 in Equation 10 to fit the data in Figure S11.

Binary oxide	$\phi_{\textbf{bin. ox.}} - \phi_{\textbf{STF}}$ **(eV)**
SiO_2	-0.14
STF	0
CaO	0.1

Binary oxide	$\phi_{\textbf{bin. ox.}} - \phi_{\textbf{PCO}}$ **(eV)**
SiO_2	-0.48
Al_2O_3	-0.23
PCO	0
Gd_2O_3	0.1
CaO	0.3
Li_2O	0.4

References

[1] M. Fátima Vaz and M.A. Fortes. Grain size distribution: The lognormal and the gamma distribution functions. *Scripta Metallurgica*, 22(1):35–40, 1988.

[2] Avner Rothschild, Wolfgang Menesklou, Harry L Tuller, E Ivers-Tiffee, and Ellen Ivers-Tiffée. Electronic structure, defect chemistry, and transport properties of SrTi1-xFexO3-y solid solutions. *Chemistry of Materials*, 18(16):3651–3659, 2006.

[3] Rotraut Merkle and Joachim Maier. Oxygen incorporation into Fe-doped SrTiO3: Mechanistic interpretation of the surface reaction. *Physical Chemistry Chemical Physics*, 4(17):4140–4148, 2002.

[4] Ting Chen, George F. Harrington, Kazunari Sasaki, and Nicola H. Perry. Impact of microstructure and crystallinity on surface exchange kinetics of strontium titanium iron oxide perovskite by: In situ optical transmission relaxation approach. *Journal of Materials Chemistry A*, 5(44):23006–23019, 2017.

[5] Nicola H. Perry, Jae Jin Kim, and Harry L. Tuller. Oxygen surface exchange kinetics measurement by simultaneous optical transmission relaxation and impedance spectroscopy: $Sr(Ti,Fe)O_{3-x}$ thin film case study. *Science and Technology of Advanced Materials*, 19(1):130–141, 2018.

[6] Emily J. Skiba, Ting Chen, and Nicola H. Perry. Simultaneous Electrical, Electrochemical, and Optical Relaxation Measurements of Oxygen Surface Exchange Coefficients: $Sr(Ti,Fe)O_{3-\delta}$ Film Crystallization Case Study. *ACS Applied Materials and Interfaces*, 12(43):48614–48630, 2020.

[7] Clement Nicollet, Cigdem Toparli, George F Harrington, Thomas Defferriere, Bilge Yildiz, and Harry L Tuller. Acidity of surface-infiltrated binary oxides as a sensitive descriptor of oxygen exchange kinetics in mixed conducting oxides. *Nature Catalysis*, 3(11):913–920, 2020.

[8] David Stroud. The effective medium approximations: Some recent developments. *Superlattices and Microstructures*, 23(3-4):567–573, 1998.

[9] Christoph Riedl, Matthäus Siebenhofer, Andreas Nenning, George E. Wilson, John Kilner, Christoph Rameshan, Andreas Limbeck, Alexander K. Opitz, Markus Kubicek, and Juergen Fleig. Surface Decorations on Mixed Ionic and Electronic Conductors: Effects on Surface Potential, Defects, and the Oxygen Exchange Kinetics. *ACS Applied Materials and Interfaces*, 15(22):26787–26798, 2023.

[10] Woo Chul Jung and Harry L. Tuller. A new model describing solid oxide fuel cell cathode kinetics: Model thin film $SrTi_{1-x}Fe_xO_{3-\delta}$ mixed conducting oxides - A case study. *Advanced Energy Materials*, 1(6):1184–1191, 2011.

[11] Veronika Metlenko, WooChul Jung, Sean Bishop, Harry L. Tuller, and Roger De Souza. Oxygen diffusion and surface exchange in the mixed conducting oxides $SrTi_{1-y}Fe_yO_{3-\delta}$. *Physical Chemistry Chemical Physics*, 4(8):1166–1169, 2016.

[12] J. Portier, P. Poizot, J. M. Tarascon, G. Campet, and M. A. Subramanian. Acid-base behavior of oxides and their electronic structure. *Solid State Sciences*, 5(5):695–699, 2003.

[13] Sean R Bishop, Todd S Stefanik, and Harry L Tuller. Electrical conductivity and defect equilibria of $Pr_{0.1}Ce_{0.9}O_{2-\delta}$. *Physical chemistry chemical physics*, 13(21):10165–10173, 2011.

[14] Melanie Kuhn, Jae Jin Kim, Sean R. Bishop, and Harry L. Tuller. Oxygen nonstoichiometry and defect chemistry of perovskite-structured $Ba_xSr_{1-x}Ti_{1-y}Fe_yO_{3-y/2+\delta}$ solid solutions. *Chemistry of Materials*, 25(15):2970–2975, 2013.

[15] Jae Jin Kim. Defect Equilibria and Electrode Kinetics in $Pr_xCe_{1-x}O_{2-\delta}$ Mixed Conducting Thin Films: An in-situ Optical and Electrochemical Investigation. *PhD thesis, Massachusetts Institute of Technology*, 2015.